Dynamic recrystallization during creep of proton-conducting barium cerate perovskites

Cristina Jiménez-Holgado and Manuel Jiménez-Melendo*

Departamento de Física de la Materia Condensada, Universidad de Sevilla. 41080 Sevilla, Spain

*Corresponding author: melendo@us.es

ABSTRACT

Uniaxial compression tests were conducted on perovskite-structured barium cerate polycrystals doped with 5 at.% yttrium and 5 at.% ytterbium and submicrometric grain sizes, at temperatures between 1423 and 1573 K (0.70-0.78T_m) and different initial strain rates. In contrast to conventional superplastic ceramics, the stress – strain curves show a pronounced and smooth stress drop before the steady state is attained. The stress level and the associated strain at the peak of the curves increase with increasing the deformation rate or decreasing the temperature. This behavior is characteristic of metallic materials with dynamic recrystallization during deformation under warm and hot conditions. Microstructural observations have shown that pre-existing twin boundaries, developed during cooling from the sintering temperature because of various crystal phase transformations, are critical in refining the grain structure through interactions with dislocations. The dependences of the peak, steady-state and critical stresses with strain rate and temperature in the present ceramics are adequately described by the constitutive equations used in metallic materials based on the Zener-Hollomon parameter and the work hardening rate.

Keywords: Creep; Perovskite; Dynamic recrystallization; Twinning

1. Introduction

Perovskite-structured oxides exhibit a wide variety of notable chemical and physical properties for valuable applications in different fields such as electrical insulation (ferroelectricity, pyroelectricity and piezoelectricity), memory devices, photovoltaic cells, catalysts, sensors, and especially as solid oxide fuel cells electrolytes due to their superior mixed electrical conductivity (electronic, proton and/or oxygen-ion) at intermediate and high temperatures [1–3]. In particular, trivalent cation-doped barium cerate $BaCe_{1-x}M_xO_{3-\delta}$ ($M = Y^{3+}$, Yb^{3+}, Nd^{3+} and Gd^{3+}, with $x \leq 0.20$ and $\delta = x/2$) exhibits one of the highest proton conductivities in humidified atmospheres because the aliovalent doping of trivalent ions at Ce^{4+}-sites introduces oxygen vacancies by charge compensation, which in turn promotes the protonic conductivity. The mechanical properties at elevated temperatures of this class of materials are therefore relevant for the selection, design and development of elements and structures in SOFCs and other high-temperature devices because creep, creep damage and mechanical degradation may decisively affect their ultimate performance under long-term operating conditions.

It has recently been reported [4] that barium cerate doped with yttrium (grain size of 0.5 μm) plastically deformed at high temperatures exhibits a ductile regime in which the stress σ – strain ε flow curves show a broad peak before reaching a prolonged steady state of deformation (secondary creep regime). This behavior, although not previously reported in other ceramic polycrystals, has been widely observed in metallic materials with dynamic recrystallization (DRX) deformed under warm and hot conditions (temperatures in the range of 0.50 to $0.90T_m$, where T_m is the melting temperature) [5,6,15–20,7–14]. In fact, DRX has been exhaustively investigated for decades in metallic materials because of its importance in controlling the microstructure in industrial forming processes. In these materials, DRX is usually revealed by a peak stress in the

σ - ε curves, whose magnitude and position are strongly temperature- and strain rate-dependent. Two main mechanisms are usually associated with DRX: discontinuous recrystallization, where the new grains nucleate and grow by a grain boundary bulging process, and continuous recrystallization (also termed rotation recrystallization), where the grain microstructure is refined by the division of the original grains along dislocation cell walls (low-angle boundaries) generated during the hardening stage, which gradually evolve towards regular, high-angle grain boundaries by dislocation absorption. Additional refinement cycles may take place during straining depending on material characteristics and deformation conditions, causing oscillatory stress peaks before reaching the steady state.

The stress drops observed recently in yttrium-doped barium cerate [4] were correlated with pre-existing twin boundaries formed in the grains during the various phase transitions that take place during the cooling process after sintering. At least three phase transformations have been reported to occur in $BaCeO_3$ [1,21]: from the high-temperature cubic phase Pm-3m to the rhombohedral symmetry R-3c at 840-880 °C, then to the orthorhombic phase Incn at 400 °C, and finally to the orthorhombic perovskite phase Pnma below 300 °C. The loss of symmetry elements during the transformation of the cubic phase into lower symmetry phases with energetically-equivalent orientational variants results systematically in twinning, as found in Y- and Nd-doped $BaCeO_3$ [22,23] and other ternary perovskite oxides such as $CaTiO_3$, $MgSiO_3$, $LaGaO_3$, $LaMnO_3$ and $BaTiO_3$ [24–29]. In Y-doped $BaCeO_3$, the pre-existing twin boundaries were found to progressively evolve towards regular grain boundaries through interaction with dislocations during deformation, fragmenting the parent grains and refining the microstructure [4]. In this regard, it is worth noting that a similar DRX mechanism, based on pre-existing twin boundary/dislocation interactions, has recently been reported in a number of metallic materials (Mg, Ti, Mg-, Ni- and Zr-alloys) [30–36], operating in the early stages of deformation in parallel with the conventional continuous or discontinuous DRX mechanisms.

Therefore, this work aims to study in detail the occurrence of DRX in barium cerates doped with different trivalent cations (yttrium and ytterbium) deformed under a wide range of experimental conditions of temperatures and strain rates. In particular, the DRX flow curves were analyzed by using the same constitutive equations used in metals, in order to assess the parallelism in the mechanical behavior of both classes of materials.

2. Experimental procedure

Polycrystalline $BaCe_{0.95}Yb_{0.05}O_{2.975}$ (5Yb-BCO) and $BaCe_{0.95}Y_{0.05}O_{2.975}$ (5Y-BCO) with relative densities of 95 ± 1 % (ρ = 6360 kg/m^3 for $BaCeO_3$) were fabricated by a conventional solid-state reaction method described elsewhere [37]. Briefly, commercial powders of $BaCO_3$, CeO_2, Yb_2O_3 and Y_2O_3 (Sigma-Aldrich, purity > 99.0%) were mixed in adequate proportions, grinded and calcined in air at 1200 °C for 10 h. X-ray diffractometry confirmed the formation of the orthorhombic perovskite structure Pnma in the calcined powders. Green pellets were obtained from these powders by uniaxial compaction at 150 MPa followed by cold isostatic pressing at 210 MPa, which were sintered in air for 10 h at 1550 °C. Powder X-ray diffraction analyses confirmed the maintenance of the perovskite phase in the sintered materials, with lattice parameters a = 6.207 Å, b = 8.800 Å and c = 6.223 Å for 5Yb-BCO, and a = 6.238 Å, b = 8.769 Å and c = 6.252 Å for 5Y-BCO (uncertainties are in the last digit); these values lie well within the range of those previously reported in acceptor-doped barium cerates [37]. These lattice parameters closely match those of undoped barium cerate (a = 6.221 Å, b = 8.781 Å and c = 6.235 Å, ICDD PDF2-2 card No. 04-006-1225) due to the similarity of the effective ionic radii of ytterbium and yttrium dopant ions with that of cerium ions (R(Ce^{4+}) = 0.87 Å, R(Yb^{3+}) = 0.87 Å, R(Y^{3+}) = 0.90 Å [38]) and the small amount of doping.

Prismatic samples of 5 × 3 x 3 mm in size were obtained from the as-fabricated pellets and compressed at constant cross-head speed in air at temperatures of 1150 - 1300 °C (0.70 – 0.78T_m, where T_m = 2016 K is the melting temperature of $BaCeO_3$) and initial strain rates $\dot{\varepsilon}_o$ between $1x10^{-6}$ and $5x10^{-4}$ s^{-1}. The experimental data, instantaneous load against time, were plotted as σ - ε curves, where σ is the true stress and ε is the true strain. The steady-state creep regime was analyzed with the standard high-temperature power law [39,40]:

$$\dot{\varepsilon} = A\,\sigma^{n}\,d^{-p}\exp\left(-Q/RT\right) \quad (1)$$

where $\dot{\varepsilon}$ is the instantaneous strain rate, A is a parameter depending on the deformation mechanism, d is the grain size, n is the stress exponent, p is the grain size exponent, Q is the activation energy for flow and R is the gas constant. The initial and deformed microstructures were analyzed by scanning (SEM) and transmission (TEM) electron microscopy on samples prepared by standard procedures.

3. Results and discussion

3.1. As-fabricated materials

Fig. 1 shows representative images of as-prepared 5Yb- and 5Y-BCO. Both materials exhibit very similar microstructures, formed by equiaxed and fine grains that follow a lognormal size distribution, as generally reported in ceramic materials [41]. The average grain size d (defined as the equivalent planar diameter) was 0.48 ± 0.22 μm and 0.55 ± 0.25 μm for 5Yb- and 5Y-BCO, respectively (uncertainties correspond to the standard deviations of the lognormal distributions). The grains were free of dislocations in both materials, with neat and straight grain

boundaries and triple points. However, planar defects corresponding to twin boundaries were found to be distributed homogeneously across the grains (marked with arrows in Figs. 1(b) and 1(d)). As noted in the Introduction, barium cerate (in general, ternary perovskite-structured oxides) is susceptible to twinning due to the different structural changes that take place during cooling after sintering [1,21]. The same twinning microstructure observed in the present 5Y- and 5Yb-BCO was reported by Cheng et al. [22,23] in 10Y- and 10Nd-BCO polycrystals synthetized by a solid-state reaction method similar to that followed in this investigation (calcination of precursor powders at 1100 °C and sintering at 1400 °C in air), as well as in $CaTiO_3$ [24], $LaGaO_3$ [27,29], and $(Ba_{1-x}Sr_x)TiO_3$ [25] ceramic perovskites.

3.2. Stress- strain flow curves

Fig. 2 shows true stress σ - true strain ε curves for 5Yb- and 5Y-BCO compressed at a fixed temperature of 1250 °C and various initial strain rates (Fig. 2(a)) and at a given strain rate of 3.2×10^{-5} s^{-1} and various temperatures (Fig. 2(b)). Compared to other fine-grained ceramics, for which the steady state of deformation is achieved almost immediately after a short hardening stage [41–45], the σ - ε curves in the present compounds exhibit a singular behavior: the stress increases up to a maximum level —the peak stress σ_P— after the work hardening stage, and then gently decreases to a minimum value —the steady-state stress σ_{ss}—, which marks the onset of the secondary creep regime[1]. The peak stress σ_P and the associated peak strain ε_P shift to higher values when decreasing the temperature T and/or increasing the initial strain rate $\dot{\varepsilon}_o$.

[1] The steady state is characterized by a rather constant slope of the stress – strain curves in constant cross-head speed tests, which decreases as $\dot{\varepsilon}_o$ decreases and/or T increases.

Furthermore, the relative height of the peak (as compared to the corresponding steady-state stress) also decreases with increasing temperature or decreasing strain rate.

These findings are phenomenologically identical to those reported in metallic materials with DRX during deformation [5,6,15–19,7–14]; for example, see Fig. 1 in Ref. [19] for an austenitic steel with an initial grain size of 18 μm compressed at temperatures between 1073 and 1323 K ($\simeq$ 0.65 - 0.80T_m) and strain rates of 10^{-4} s^{-1} to 10^{-2} s^{-1}. In metallic materials, dynamic recrystallization is caused by the appearance of new grains by the strain-induced bulging of the original grain boundaries (discontinuous recrystallization, as found in Ni, Ti, Mg and austenitic Fe) or by the progressive division of the parent grains along the dislocation walls (subgrains) formed during hardening (continuous recrystallization, as reported in Al, β-Ti alloys and ferritic steels).

3.3. Microstructure of deformation

Fig. 3 displays the microstructure of a 50%-strained 5Yb-BCO sample. Despite the large strain achieved, no signs of cavitation were observed, with the grains remaining equiaxed. These features suggest that grain boundary sliding is the dominant deformation mechanism, as generally reported in the creep of superplastic metallic and ceramic materials [41–46]. Furthermore, SEM image analysis measurements have shown a decrease of about 20% in the final grain size, indicating the occurrence of grain fragmentation during testing. These new and smaller grains are uniformly dispersed throughout the material volume, as can be clearly observed in Fig. 3(a), and account for the presence of the peak stress in the σ - ε curves. The same microstructural evolution was found at the other testing conditions, with reductions in the average grain size of about 20% (experimental uncertainties of 5%) after 50%-deformation. This result is consistent

with the establishment of a common twin-boundary network in the grains prior to deformation, which was developed during cooling after the sintering process. In contrast to undeformed samples, TEM observations have revealed an intense dislocation activity in the strained samples (Fig. 3(b)), with numerous dislocations distributed mainly along the twin boundaries and nearby areas. This dislocation-twin boundary interaction caused the progressive fragmentation of the parent grains (Fig. 3(c)), initiating the softening stage. The same deformation microstructure was observed in 5Y-BCO samples tested under similar experimental conditions, which has been reported elsewhere [4].

In this regard, it should be noted that, although continuous and discontinuous DRX are the main mechanisms for strain softening in metals, a twin-assisted DRX mechanism has recently been reported in various metals and metallic alloys (Mg, Ti, Zr, Ni and austenitic steel alloys [30–36]) which contributes to the overall restoration process during hot deformation. In these materials, pre-existing twin boundaries were found to turn progressively into high-angle, regular grain boundaries through interaction with dislocations during deformation, dividing the original grains and promoting the softening stage, as observed in the present ceramics.

3.4. Analysis of the flow curves

3.4.1. Steady-state regime

In fine-grained superplastic materials, a steady state of deformation is readily achieved after a very short (ε < 5%) transient hardening stage [41–45]. In the current cerates, however, the hardening stage is followed by a broad and gentle stress drop before reaching the steady state (Fig. 2), as found in metals with single-peak DRX behavior in which the secondary creep regime

corresponds, once the final microstructure is established, to a balance between the production of dislocations created by the applied stress and the annihilation (usually by climb) of such dislocations, resulting in a plateau in the σ - ε curves. Fundamental creep models based on such dislocation-recovery mechanisms predict a stress exponent n (Eq. (1)) of 3 and greater [39,40,47]; experimental values of n for most metals with initial grain sizes of several tents of micrometers are usually in the range of 4 to 8 [39,47].

In contrast, a stress exponent n of 2 has generally been reported in the creep of superplastic metallic and ceramic materials [41–46], for which the morphological characteristics of the grains remain essentially unchanged after extended steady states of deformation. In such conditions, grain boundary sliding (GBS) is the major deformation mechanism, where individual grains slide and rotate relative to each other to accommodate the overall deformation of the material. Most of the theoretical and semiphenomenological models based on GBS predict a stress exponent n = 2 [39,44] in agreement with the experimental results, although the microscopic details of the process are still a matter of debate. In general, dislocations multiply and move along grain boundaries under the applied stress at the very early stage of deformation, which are blocked at grain boundary irregularities (mainly triple points) as the strain proceeds, initiating the hardening stage. A recovery mechanism, usually called the relaxation or accommodation mechanism, rapidly balances hardening to achieve the steady state. Different relaxation processes —which are indeed the rate-controlling mechanism— have been proposed: grain boundary migration, diffusional flow, interface-reaction-controlled-diffusion, intergranular and/or intragranular dislocation motion processes, etc. [39,44]. Under such conditions, the activation energy Q (Eq. (1)) is commonly associated with the bulk or grain boundary self-diffusion energy.

The true stress exponent n in the current cerates was determined from the variation of the initial strain rate with steady-state stress σ_{ss} at different temperatures (Fig. 4(a)). A weighted average value of n = 1.96 ± 0.16 was estimated from the slopes of the best fit lines, regardless of doping, in excellent agreement with the experimental value of 2 found in superplastic materials. Similarly, the activation energy Q for steady state was estimated from the variation of steady-state stress σ_{ss} with reciprocal absolute temperature (Fig. 4(b)), resulting in an average value of Q = 440 ± 40 kJ/mol for both compounds. The same energy was measured by conducting temperature stepping experiments at constant load (creep tests), as shown in Fig. 5 for a sample of 5Yb-BCO tested at 50 MPa and temperatures of 1200 and 1240 °C. This plot additionally shows that flow softening (corresponding to an increase in strain rate in this kind of tests) appears at the beginning of the initial stage after loading, whereas the following stages easily attain the steady state without transients. This result is consistent with the presence of a single peak in the σ - ε curves (Fig. 2), and indicates that the grain fragmentation induced by twinning is mostly completed once the softening stage is ended.

As noted above, the value of Q can be ascribed to the lattice or grain boundary diffusion energy. In compounds, the diffusion energy is a rather complicated magnitude that involves the diffusion of the various atomic species along different diffusion paths; in simple cases, Q reduces to that of the slowest diffusion species moving along the faster path. Unfortunately, there are no enough diffusion studies on barium cerate for a proper determination of the ionic species that controls the deformation rate. Only the bulk self-diffusion energy of oxygen Q = 60-100 kJ/mol has been reported [48], significantly lower than the value found in this study, suggesting that cation diffusion is the rate-controlling step during the steady-state creep.

It is worth noting that the 20 %-reduction in grain size measured in the cerates between the initial and final microstructures is enough to explain the noticeable stress drops in the σ - ε curves (Fig. 2) due to the combined effect of the strong dependence with grain size and the weak dependence with stress of the steady-state strain rate in superplastic materials, for which p = 2 - 3 and n = 2, respectively, in Eq. (1) [42,44,45]. These dependences are significantly different from those found in large-grained materials, where p is nearly zero and n ranges between 4 and 8 [39,40,47]. The stress peaks are thus less obvious in metallic materials despite grain size reductions of more than one order of magnitude are commonly reported [5,49,50].

3.4.2. Stress peak

At relatively low stresses, the temperature and strain rate dependence of the peak stress in metals is usually analyzed with the power law [7,13,51]

$$Z = \dot{\varepsilon} \exp\left(Q'/RT\right) = A'\sigma_p^{n'} \quad (2)$$

where Z is the Zener-Hollomon parameter (the temperature-compensated strain rate), A' is a material constant, and n' and Q' are the stress coefficient and the activation energy, respectively, for peak stress. In metals, these parameters have values very similar to, but should not be confused with, the true creep parameters n and Q for steady-state deformation (Eq. (1)), with n' varying between 4 and 10 and Q' close to the diffusion energy [12,13,51,52], indicating that the peak stress is again related to a dislocation recovery-controlled process.

Following the same procedure used in metals (Eq. 2), Fig. 6 displays the variation of the Zener-Hollomon parameter Z with peak stress for the cerates at the temperatures and strain rates studied. Treating the results of both compounds as a single data set because of their rather

similar mechanical behavior (the difference in strain rate is less than a factor of 2, Fig. 4(a)), a least-squares best fit leads to the constitutive equation

$$Z = 1.30x10^{8}\ \sigma_P^{1.71}\ (s^{-1}) \quad (3)$$

with σ_p in MPa. The mean stress coefficient n' = 1.71 ± 0.12 estimated from the fit is similar to the true stress exponent n measured under steady-state conditions (Fig. 4(a)), following the same trend observed in metals. In the previous analysis (Eq. (2)), the true strain rate $\dot{\varepsilon}$ was replaced by the initial strain rate $\dot{\varepsilon}_o$. It can be easily shown, however, that both rates are related by $\dot{\varepsilon}(\varepsilon) = \exp(-\varepsilon).\dot{\varepsilon}_o$ in a constant cross-head speed test, and because the peak strains at which the peak stresses appear are very modest $\varepsilon_P \leq 5\%$ (Fig. 2), the difference is very slight $\dot{\varepsilon}(\varepsilon_P) \leq 1.05\dot{\varepsilon}_o$ and justifies the above substitution.

3.4.3. Initiation of dynamic recrystallization

During strain hardening, a critical microstructural condition is reached before the appearance of the peak stress, which marks the onset of DRX. Due to the importance of these critical stress σ_{cr} and critical strain ε_{cr} in metal industrial forming processes, they have been widely investigated over decades; critical stresses σ_{cr} reported in metallic materials are typically in the range of 0.5 - 0.8σ_P. According to the literature [53–58], σ_{cr} can be found from the variation of the work hardening rate $\theta = d\sigma/d\varepsilon$ with stress σ, which also allows the identification of the peak and steady-state stresses and strains. Examples of such plots are shown in Fig. 7 for 5Y- and 5Yb-BCO deformed at 1250 °C and 1.7x10^{-4} s^{-1} (Fig. 2). The shape of these θ - σ and θ -ε curves again resembles closely those reported for metals with DRX (see, for example, Fig. 1 of Ref. [20], Fig. 5(b) of Ref. [58], and Fig. 7 of Ref. [49]). These plots yield to critical stresses of $\sigma_{cr} \simeq 0.65$ - 0.70σ_P, which is within the range reported for metals. Additionally, Fig. 7(b) shows that both the peak strain ε_P

and the steady-state strain ε_{ss} increase with increasing the creep resistance of the material under the same experimental conditions of deformation, as also reported in metallic materials.

4. CONCLUSIONS

The mechanical behavior of fine-grained (d = 0.5 μm) barium cerate polycrystals doped with 5 at.% yttrium and 5 at.% ytterbium have been investigated at temperatures of 1150 - 1300 °C (0.70 - 0.78T_m) by means of uniaxial compression tests performed at constant initial strain rate and microstructural analyses. Both compounds have the same initial microstructure, composed of equiaxed and submicrometric-sized grains, free of dislocations and with multiple twin boundaries produced by the different phase transformations that the compounds undergo upon cooling from sintering.

The σ - ε curves exhibit a single peak stress behavior, characterized by a softening stage before reaching the steady state. The deformation variables, initial strain rate $\dot{\varepsilon}_o$ and temperature T, have a strong effect on the peak stress, which increases with decreasing T and increasing $\dot{\varepsilon}_o$. This behavior is qualitatively similar to that found in metallic materials with dynamic recrystallization during warm and hot deformation. Pre-existing twin boundaries in 5Yb- and 5Y-BCO play the same role as polygonized dislocation walls in metals, which progressively turn into conventional grain boundaries by dislocation absorption during deformation, fragmenting the original grains.

The maintenance of the initial equiaxed shape of the grains after 50%-straining, together with the true stress exponent n of 2 measured under steady-state conditions, indicate that the plastic

deformation of both compounds is accomplished by grain boundary sliding, as reported in superplastic ceramic and metallic materials. A true activation energy of 440 kJ/mol was estimated, which is likely to represent the cation diffusion energy.

The peak stress and strain behavior was analyzed by using the constitutive equations derived for metals based on the Zener-Hollomon parameter, resulting in a stress coefficient n' close to n, in agreement with the trend observed in metallic materials. Furthermore, the critical stress σ_{cr} for initiation of DRX was estimated from the variation of the work hardening rate with stress, resulting $\sigma_{cr} \simeq 0.75\sigma_P$, which is in the range of values reported for metals. These results show that, although the individual deformation mechanisms in metals are different from those in the present ceramics, their overall mechanical behavior can be analyzed using the same approaches.

Acknowledgment

This work was supported by Project no. MAT2009-13979-C03-01, Ministerio de Ciencia e Innovación, Spain. The assistance provided by Dr. Cristina Vaquero is appreciated.

REFERENCES

1. Medvedev, D. *et al.* BaCeO3: Materials development, properties and application. *Progress in Materials Science* vol. 60 72–129 (2014).
2. Ito, N. Intermediate-Temperature SOFCs Using Proton-Conducting Perovskite. 273–283 (2009) doi:10.1007/978-0-387-77708-5_14.
3. Kreuer, K. D. Proton-Conducting Oxides. *Annu. Rev. Mater. Res.* **33**, 333–359 (2003).
4. Jiménez-Melendo, M. & Jiménez-Holgado, C. Metal-like peak stress behavior of yttrium-doped BaCeO3 ceramic. *J. Eur. Ceram. Soc.* (2022) doi:10.1016/J.JEURCERAMSOC.2022.03.002.
5. Sakai, T. & Jonas, J. J. Overview no. 35 Dynamic recrystallization: Mechanical and microstructural considerations. *Acta Metall.* **32**, 189–209 (1984).
6. Sakai, T., Belyakov, A., Kaibyshev, R., Miura, H. & Jonas, J. J. Dynamic and post-dynamic recrystallization under hot, cold and severe plastic deformation conditions. *Progress in Materials Science* vol. 60 130–207 (2014).
7. McQueen, H. J. & Ryan, N. D. Constitutive analysis in hot working. *Mater. Sci. Eng. A* **322**, 43–63 (2002).
8. Graetz, K., Miessen, C. & Gottstein, G. Analysis of steady-state dynamic recrystallization. *Acta Mater.* **67**, 58–66 (2014).
9. Varela-Castro, G., Cabrera, J. M. & Prado, J. M. Critical strain for dynamic recrystallisation. The particular case of steels. *Metals (Basel).* **10**, (2020).
10. Sitdikov, O. & Kaibyshev, R. Dynamic recrystallization in pure magnesium. *Mater. Trans.* **42**, 1928–1937 (2001).
11. Guo, Q., Li, D., Guo, S., Peng, H. & Hu, J. The effect of deformation temperature on the microstructure evolution of Inconel 625 superalloy. *J. Nucl. Mater.* **414**, 440–450 (2011).
12. Lin, Y. C., Chen, M. S. & Zhong, J. Prediction of 42CrMo steel flow stress at high

temperature and strain rate. *Mech. Res. Commun.* **35**, 142–150 (2008).

13. Liu, J., Cui, Z. & Li, C. Modelling of flow stress characterizing dynamic recrystallization for magnesium alloy AZ31B. *Comput. Mater. Sci.* **41**, 375–382 (2008).
14. Ji, H. *et al.* Optimization the working parameters of as-forged 42CrMo steel by constitutive equation-dynamic recrystallization equation and processing maps. *J. Mater. Res. Technol.* **9**, 7210–7224 (2020).
15. Wu, H. yu, Yang, J. chen, Liao, J. hao & Zhu, F. jun. Dynamic behavior of extruded AZ61 Mg alloy during hot compression. *Mater. Sci. Eng. A* **535**, 68–75 (2012).
16. Gourdet, S. & Montheillet, F. An experimental study of the recrystallization mechanism during hot deformation of aluminium. *Mater. Sci. Eng. A* **283**, 274–288 (2000).
17. Gourdet, S. & Montheillet, F. A model of continuous dynamic recrystallization. *Acta Mater.* **51**, 2685–2699 (2003).
18. Sakai, T., Miura, H., Goloborodko, A. & Sitdikov, O. Continuous dynamic recrystallization during the transient severe deformation of aluminum alloy 7475. *Acta Mater.* **57**, 153–162 (2009).
19. Dolzhenko, P., Tikhonova, M., Kaibyshev, R. & Belyakov, A. Dynamically Recrystallized Microstructures, Textures, and Tensile Properties of a Hot Worked High-Mn Steel. *Met. 2019, Vol. 9, Page 30* **9**, 30 (2019).
20. Mirzadeh, H., Cabrera, J. M., Prado, J. M. & Najafizadeh, A. Hot deformation behavior of a medium carbon microalloyed steel. *Mater. Sci. Eng. A* **528**, 3876–3882 (2011).
21. Knight, K. S. Powder neutron diffraction studies of BaCe0.9Y0.1O2.95 and BaCeO3 at 4.2 K: A possible structural site for the proton. *Solid State Ionics* **127**, 43–48 (2000).
22. Cheng, S. Y., Ho, N. J. & Lu, H. Y. Phase-transformation-induced anti-phase boundary domains in barium cerate perovskite. *J. Am. Ceram. Soc.* **89**, 3498–3506 (2006).
23. Cheng, S. Y., Ho, N. J. & Lu, H. Y. Phase-transformation-induced twinning in orthorhombic BaCeO3. *J. Am. Ceram. Soc.* **91**, 2298–2303 (2008).

24. Wang, Y. & Liebermann, R. C. Electron microscopy study of domain structure due to phase transitions in natural perovskite. *Phys. Chem. Miner.* **20**, 147–158 (1993).

25. Lee, B. K., Jung, Y. Il, Kang, S. J. L. & Nowotny, J. {111} twin formation and abnormal grain growth in barium strontium titanate. *J. Am. Ceram. Soc.* **86**, 155–160 (2003).

26. Pramanik, S., Ravikumar, K., Kalsar, R., Suwas, S. & Basu, B. On the orientation relationships in phase transformation of CaTiO3. *Ceram. Int.* **45**, 12509–12515 (2019).

27. Wang, W. L. & Lu, H. Y. Phase-transformation-induced twinning in orthorhombic LaGaO 3: {121} And [010] twins. in *Journal of the American Ceramic Society* vol. 89 281–291 (John Wiley & Sons, Ltd, 2006).

28. Wang, Y., Guyot, F., Yeganeh-Haeri, A. & Liebermann, R. C. Twinning in MgSiO3 perovskite. *Science (80-.).* **248**, 468–471 (1990).

29. Wang, W. L. & Lu, H. Y. Twinning induced by the rhombohedral to orthorhombic phase transition in lanthanum gallate (LaGaO3). *Phys. Chem. Miner.* **33**, 435–444 (2006).

30. Chen, W., Jia, C., Hu, B., Zheng, C. & Li, D. Evolution of twins and sub-boundaries at the early stage of dynamic recrystallization in a Ni-30%Fe austenitic model alloy. *Mater. Sci. Eng. A* **733**, 419–428 (2018).

31. Li, S. *et al.* Twinning behaviors and grain refinement mechanisms during friction stir processing of Zr alloy. *Mater. Charact.* **163**, 110277 (2020).

32. Ma, Q., Li, B., Marin, E. B. & Horstemeyer, S. J. Twinning-induced dynamic recrystallization in a magnesium alloy extruded at 450 °c. *Scr. Mater.* **65**, 823–826 (2011).

33. Yan, C. K. *et al.* Dynamic recrystallization of titanium: Effect of pre-activated twinning at cryogenic temperature. *Acta Mater.* **154**, 311–324 (2018).

34. Yu, Z. & Choo, H. Influence of twinning on the grain refinement during high-temperature deformation in a magnesium alloy. *Scr. Mater.* **64**, 434–437 (2011).

35. Beladi, H., Cizek, P. & Hodgson, P. D. Dynamic Recrystallization of Austenite in Ni-30 Pct

Fe Model Alloy: Microstructure and Texture Evolution. *Metall. Mater. Trans. A 2009 405* **40**, 1175–1189 (2009).

36. Sitdikov, O., Kaibyshev, R. & Sakai, T. Dynamic recrystallization based on twinning in coarse-grained Mg. in *Materials Science Forum* vols 419–422 521–526 (Trans Tech Publications Ltd, 2003).

37. Vaquero-Aguilar, C. & Jiménez-Melendo, M. Characterization and creep properties of proton-conducting Yb-doped barium cerate. *J. Eur. Ceram. Soc.* **31**, 2671–2676 (2011).

38. Shannon, R. D. & IUCr. Revised effective ionic radii and systematic studies of interatomic distances in halides and chalcogenides. *urn:issn:0567-7394* **32**, 751–767 (1976).

39. Poirier, J.-P. *Creep of Crystals*. *Creep of Crystals* (Cambridge University Press, 1985). doi:10.1017/CBO9780511564451.

40. Bretheau, T., Castaing, J., Rabier, J. & Veyssière, P. Dislocation motion and high temperature plasticity of binary and ternary oxides. *Adv. Phys.* **28**, 835–1014 (1979).

41. Ciria, D., Jiménez-Melendo, M., Aubin, V. & Dezanneau, G. Creep properties of high dense La9.33Si6O26 electrolyte for SOFCs. *J. Eur. Ceram. Soc.* **40**, 1989–1998 (2020).

42. Jiménez-Melendo, M., Domínguez-Rodríguez, A. & Bravo-León, A. Superplastic flow of fine-grained yttria-stabilized zirconia polycrystals: Constitutive equation and deformation mechanisms. *J. Am. Ceram. Soc.* **81**, 2761–2776 (1998).

43. Ciria, D., Jiménez-Melendo, M., Aubin, V. & Dezanneau, G. High-temperature mechanical behavior of proton-conducting yttrium-doped barium zirconate perovskite. *J. Eur. Ceram. Soc.* **41**, 1374–1383 (2021).

44. Nieh, T. G., Wadsworth, J. & Sherby, O. D. *Superplasticity in Metals and Ceramics*. (Cambridge University Press, 1997). doi:10.1017/CBO9780511525230.

45. WAKAI, F., SAKAGUCHI, S. & MATSUNO, Y. Superplasticity of Yttria-Stabilized Tetragonal ZrO2 Polycrystals. *Adv. Ceram. Mater.* **1**, 259–263 (1986).

46. Alabort, E., Kontis, P., Barba, D., Dragnevski, K. & Reed, R. C. On the mechanisms of superplasticity in Ti-6Al-4V. *Acta Mater.* **105**, 449–463 (2016).

47. Kassner, M. E. Fundamentals of Creep in Metals and Alloys. *Fundam. Creep Met. Alloy.* (2008) doi:10.1016/B978-0-08-047561-5.X0001-2.

48. Bonanos, N. Transport study of the solid electrolyte BaCe0.9Gd0.1O2.95 at high temperatures. *J. Phys. Chem. Solids* **54**, 867–870 (1993).

49. Mirzadeh, H. & Najafizadeh, A. Hot Deformation and Dynamic Recrystallization of 17-4 PH Stainless Steel. *ISIJ Int.* **53**, 680–689 (2013).

50. Ion, S. E., Humphreys, F. J. & White, S. H. Dynamic recrystallisation and the development of microstructure during the high temperature deformation of magnesium. *Acta Metall.* **30**, 1909–1919 (1982).

51. Wang, L., Liu, F., Cheng, J. J., Zuo, Q. & Chen, C. F. Hot deformation characteristics and processing map analysis for Nickel-based corrosion resistant alloy. *J. Alloys Compd.* **623**, 69–78 (2015).

52. Solhjoo, S. Determination of critical strain for initiation of dynamic recrystallization. *Mater. Des.* **31**, 1360–1364 (2010).

53. Poliak, E. I. & Jonas, J. J. A one-parameter approach to determining the critical conditions for the initiation of dynamic recrystallization. *Acta Mater.* **44**, 127–136 (1996).

54. Poliak, E. I. & Jonas, J. J. Initiation of dynamic recrystallization in constant strain rate hot deformation. *ISIJ Int.* **43**, 684–691 (2003).

55. Mirzadeh, H., Parsa, M. H. & Ohadi, D. Hot deformation behavior of austenitic stainless steel for a wide range of initial grain size. *Mater. Sci. Eng. A* **569**, 54–60 (2013).

56. Najafizadeh, A. & Jonas, J. J. Predicting the Critical Stress for Initiation of Dynamic Recrystallization. *ISIJ Int.* **46**, 1679–1684 (2006).

57. Ryan, N. D. & McQueen, H. J. Flow stress, dynamic restoration, strain hardening and

ductility in hot working of 316 steel. *J. Mater. Process. Technol.* **21**, 177–199 (1990).

58. Hu, Z. & Wang, K. Evolution of Dynamic Recrystallization in 5CrNiMoV Steel during Hot Forming. *Adv. Mater. Sci. Eng.* **2020**, (2020).

FIGURE CAPTIONS

Fig. 1. SEM and TEM images of as-fabricated 5Yb-BCO (a,b) and 5Y-BCO (c,d). Both microstructures are essentially identical, with equiaxed and submicrometer-sized grains, free of dislocations and with phase transformation-induced twin boundaries (some are marked with arrows).

Fig. 2. Variation of flow stress with strain in 5Y- and 5Yb-BCO deformed (a) at 1250 °C and different initial strain rates, and (b) different temperatures at a fixed initial strain rate of 3.2×10^{-5} s^{-1}. The curves resemble the typical behavior observed in metallic materials with dynamic recrystallization.

Fig. 3. Microstructure of 5Yb-BCO sample deformed up to 50% at $\dot{\varepsilon}_o = 1.6 \times 10^{-4} s^{-1}$ and T = 1250 °C. SEM image showing the presence of new, finer-sized grains (a). TEM images showing a high dislocation activity inside the grains (b), which resulted in the gradual division of the parent grains along the pre-existing twin boundaries (c).

Fig. 4. (a) Variation of the initial strain rate $\dot{\varepsilon}_o$ with steady-state stress σ_{ss} for 5Yb- and 5Y-BCO deformed at different temperatures; and (b) variation of σ_{ss} with reciprocal absolute temperature at different strain rates. Weighted average values of the stress exponent n = 1.96 ± 0.16 and the activation energy Q = 440 ± 40 kJ/mol were estimated from best-fit regression lines.

Fig. 5. Creep curve at constant load for 5Yb-BCO plotted as log $\dot{\varepsilon}$ vs ε showing several temperatures changes to measure the activation energy Q. Softening is observed only at the

initial deformation stage, indicating a single peak stress DRX behavior.

Fig. 6. Variation of the Zener-Hollomon parameter Z with peak stress for 5Y- and 5Yb-BCO deformed between 1150 and 1300 °C. The stress coefficient n' estimated from linear regression is n' = 1.71 ± 0.12.

Fig. 7. Variation of the work hardening rate with (a) stress and (b) strain, for 5Y- and 5Yb-BCO deformed at 1250 °C and 1.7×10^{-4} s^{-1} (Fig. 2). The characteristic points of the curves are marked.

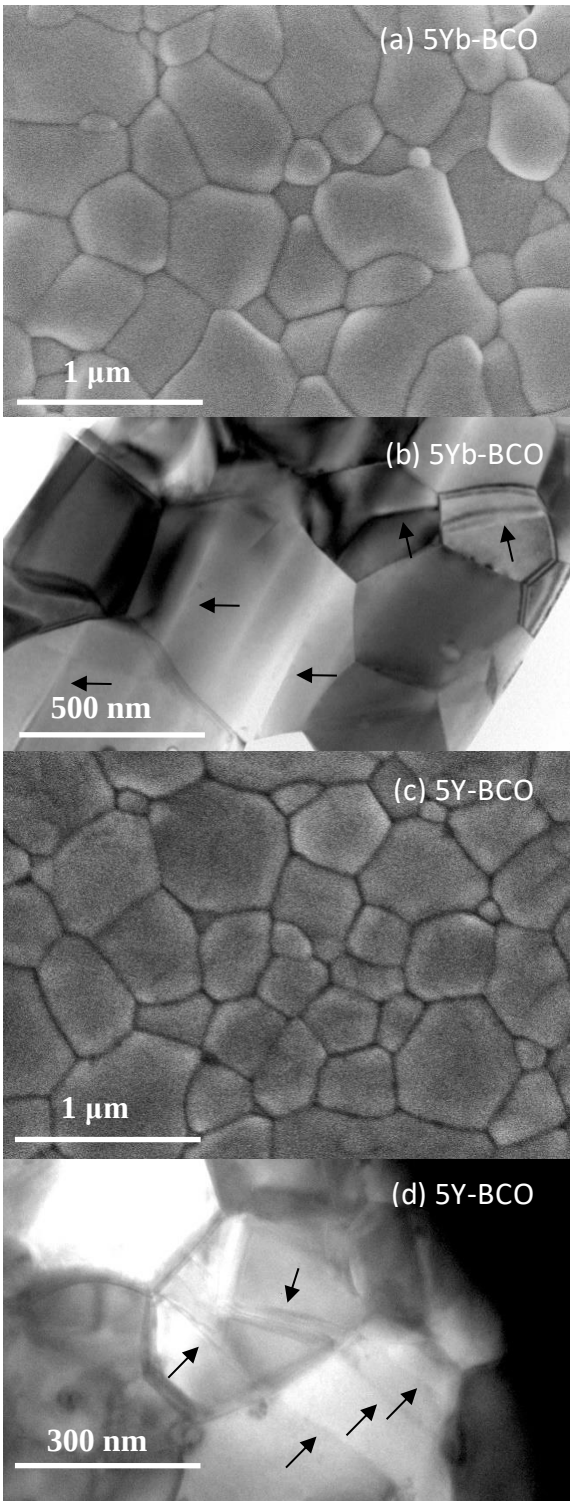

Fig. 1

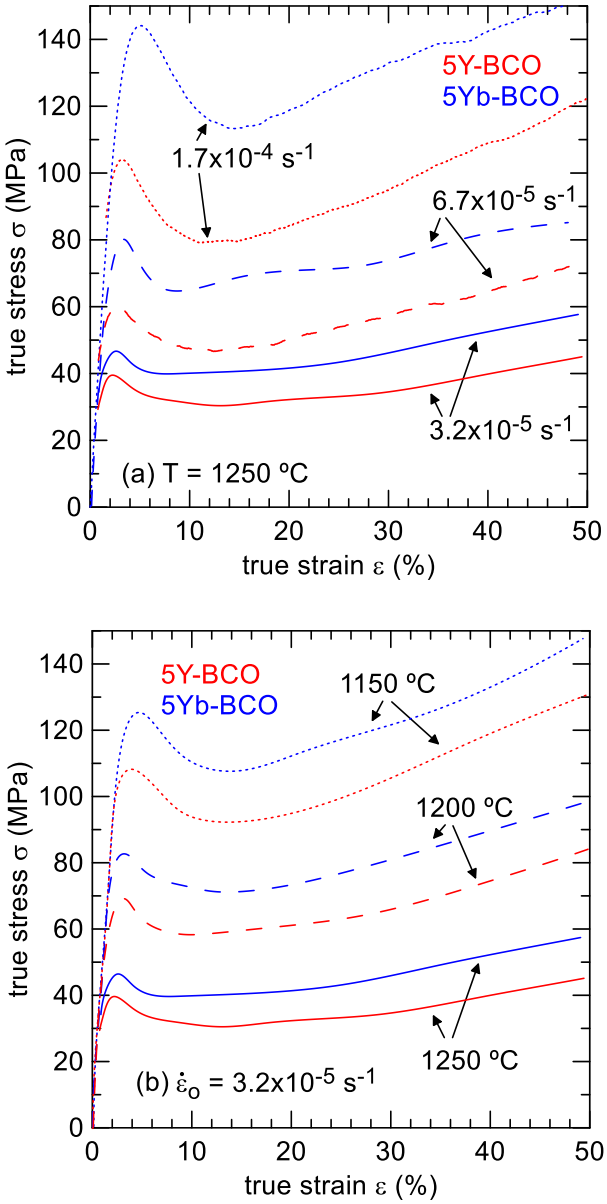
5Y-BCO
5Yb-BCO
1.7x10-4 s-1
6.7x10-5 s-1
3.2x10-5 s-1
(a) T = 1250 ºC
true stress σ (MPa)
true strain ε (%)
1150 ºC
1200 ºC
1250 ºC
(b) ε̇o = 3.2x10-5 s-1

Fig. 2

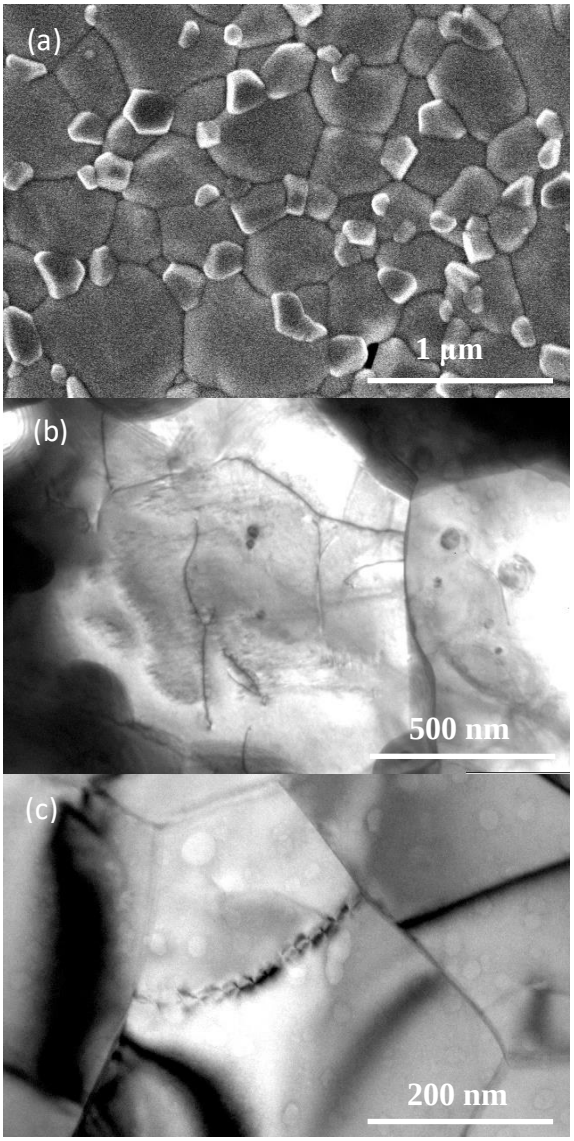

Fig. 3

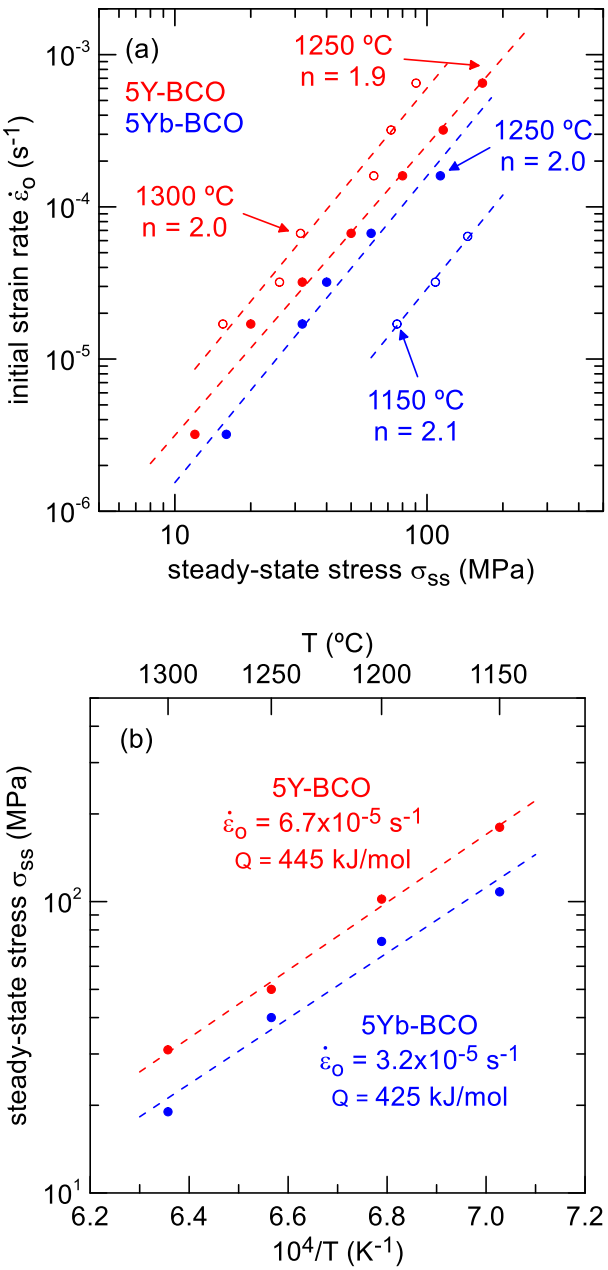
(a)
5Y-BCO
5Yb-BCO
1250 ºC
n = 1.9
1250 ºC
n = 2.0
1300 ºC
n = 2.0
1150 ºC
n = 2.1
initial strain rate $\dot{\varepsilon}_o$ (s^{-1})
steady-state stress σ_{ss} (MPa)
T (ºC)
1300
1250
1200
1150
(b)
5Y-BCO
$\dot{\varepsilon}_o$ = 6.7x10^{-5} s^{-1}
Q = 445 kJ/mol
5Yb-BCO
$\dot{\varepsilon}_o$ = 3.2x10^{-5} s^{-1}
Q = 425 kJ/mol
steady-state stress σ_{ss} (MPa)
10^4/T (K^{-1})

Fig. 4

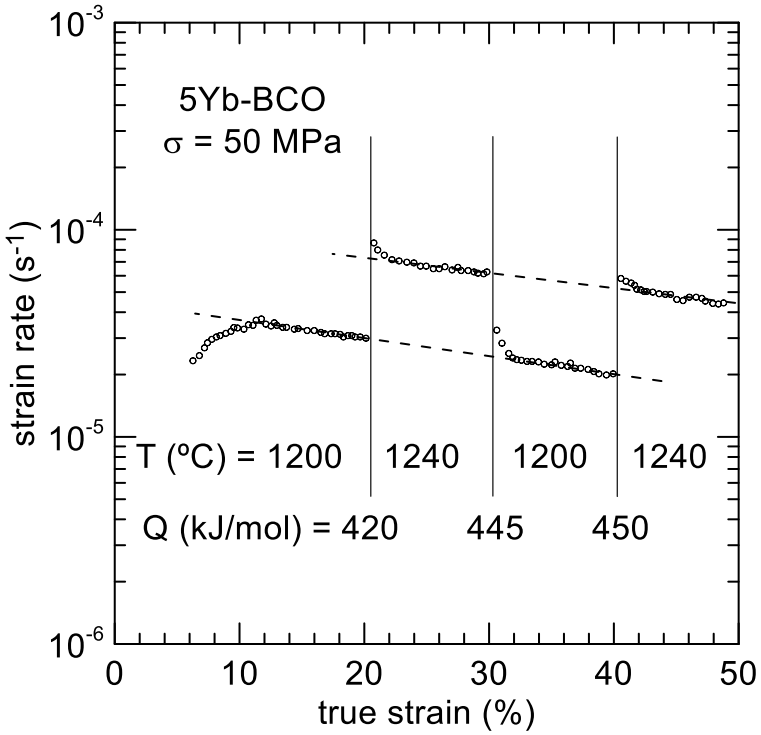
5Yb-BCO
σ = 50 MPa
T (ºC) = 1200
1240
1200
1240
Q (kJ/mol) = 420
445
450
strain rate (s-1)
true strain (%)
10-3
10-4
10-5
10-6
0
10
20
30
40
50

Fig. 5

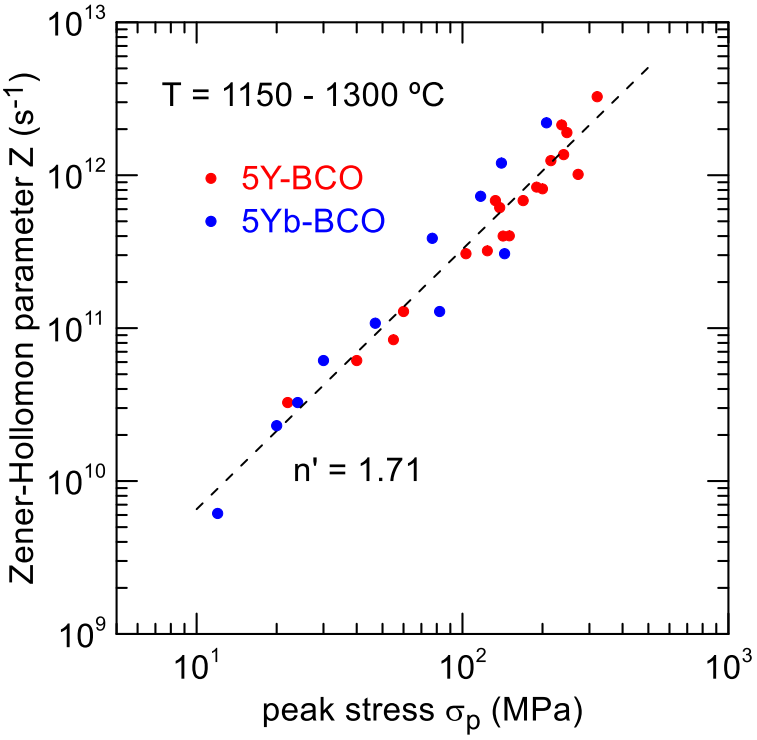
T = 1150 - 1300 ºC
5Y-BCO
5Yb-BCO
n' = 1.71
Zener-Hollomon parameter Z (s-1)
peak stress σp (MPa)
10^13
10^12
10^11
10^10
10^9
10^1
10^2
10^3

Fig. 6

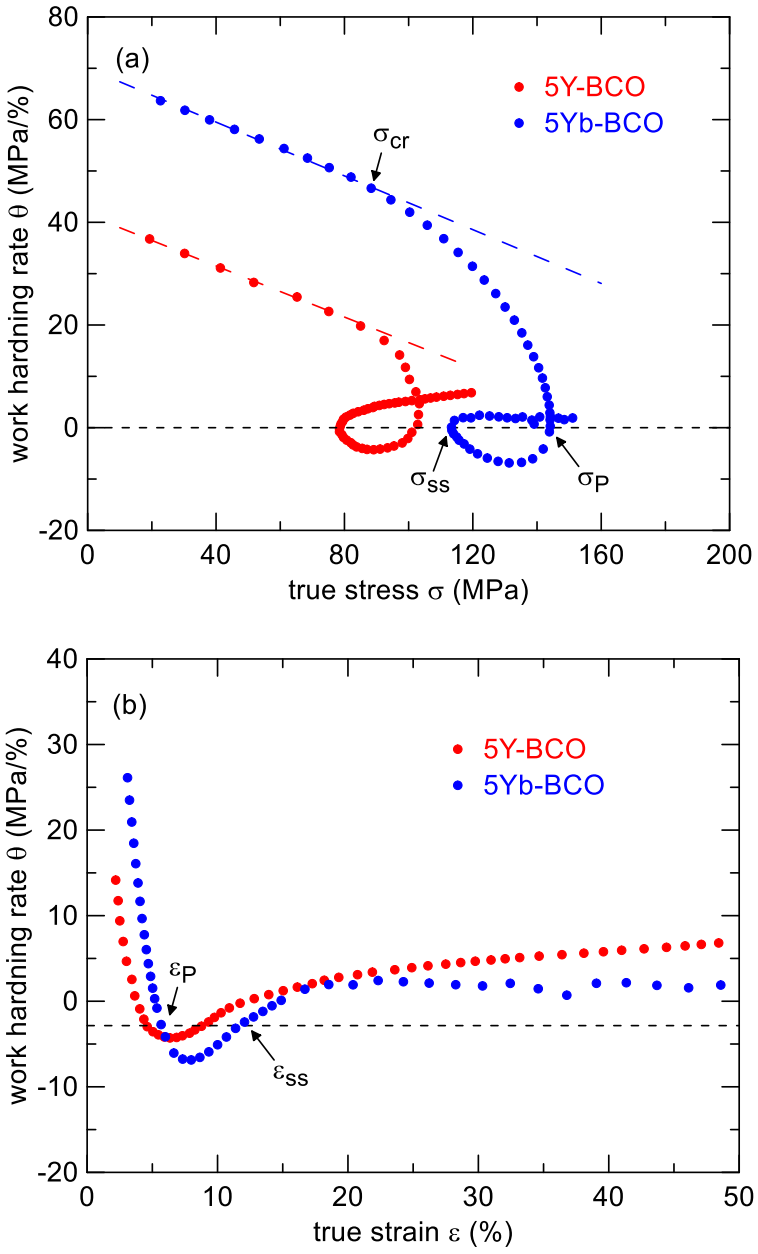
(a)
5Y-BCO
5Yb-BCO
σcr
σss
σP
work hardning rate θ (MPa/%)
true stress σ (MPa)
(b)
5Y-BCO
5Yb-BCO
εP
εss
work hardning rate θ (MPa/%)
true strain ε (%)

Fig. 7